hep-ex/9506002 v2   5 Jun 1995

Measurement of the e^+ and e^- induced charged current cross sections at HERA

H1 Collaboration

Abstract:

The cross sections for the charged current processes $e^- p \to \nu_e +$ hadrons and, for the first time, $e^+ p \to \overline{\nu}_e +$ hadrons are measured at HERA for transverse momenta larger than $25\,\mathrm{GeV}$.

H1 Collaboration

S. Aid[13], V. Andreev[25], B. Andrieu[28], R.-D. Appuhn[11], M. Arpagaus[36], A. Babaev[24], J. Bähr[35], J. Bán[17], Y. Ban[27], P. Baranov[25], E. Barrelet[29], R. Barschke[11], W. Bartel[11], M. Barth[4], U. Bassler[29], H.P. Beck[37], H.-J. Behrend[11], A. Belousov[25], Ch. Berger[1], G. Bernardi[29], R. Bernet[36], G. Bertrand-Coremans[4], M. Besançon[9], R. Beyer[11], P. Biddulph[22], P. Bispham[22], J.C. Bizot[27], V. Blobel[13], K. Borras[8], F. Botterweck[4], V. Boudry[7], A. Braemer[14], F. Brasse[11], W. Braunschweig[1], V. Brisson[27], D. Bruncko[17], C. Brune[15], R. Buchholz[11], L. Büngener[13], J. Bürger[11], F.W. Büsser[13], A. Buniatian[11,38], S. Burke[18], M.J. Burton[22], G. Buschhorn[26], A.J. Campbell[11], T. Carli[26], F. Charles[11], M. Charlet[11], D. Clarke[5], A.B. Clegg[18], B. Clerbaux[4], M. Colombo[8], J.G. Contreras[8], C. Cormack[19], J.A. Coughlan[5], A. Courau[27], Ch. Coutures[9], G. Cozzika[9], L. Criegee[11], D.G. Cussans[5], J. Cvach[30], S. Dagoret[29], J.B. Dainton[19], W.D. Dau[16], K. Daum[34], M. David[9], B. Delcourt[27], L. Del Buono[29], A. De Roeck[11], E.A. De Wolf[4], P. Di Nezza[32], C. Dollfus[37], J.D. Dowell[3], H.B. Dreis[2], A. Droutskoi[24], J. Duboc[29], D. Düllmann[13], O. Dünger[13], H. Duhm[12], J. Ebert[34], T.R. Ebert[19], G. Eckerlin[11], V. Efremenko[24], S. Egli[37], H. Ehrlichmann[35], S. Eichenberger[37], R. Eichler[36], F. Eisele[14], E. Eisenhandler[20], R.J. Ellison[22], E. Elsen[11], M. Erdmann[14], W. Erdmann[36], E. Evrard[4], L. Favart[4], A. Fedotov[24], D. Feeken[13], R. Felst[11], J. Feltesse[9], J. Ferencei[15], F. Ferrarotto[32], K. Flamm[11], M. Fleischer[26], M. Flieser[26], G. Flügge[2], A. Fomenko[25], B. Fominykh[24], M. Forbush[7], J. Formánek[31], J.M. Foster[22], G. Franke[11], E. Fretwurst[12], E. Gabathuler[19], K. Gabathuler[33], J. Garvey[3], J. Gayler[11], M. Gebauer[8], A. Gellrich[11], H. Genzel[1], R. Gerhards[11], A. Glazov[35], U. Goerlach[11], L. Goerlich[6], N. Gogitidze[25], M. Goldberg[29], D. Goldner[8], B. Gonzalez-Pineiro[29], I. Gorelov[24], P. Goritchev[24], C. Grab[36], H. Grässler[2], R. Grässler[2], T. Greenshaw[19], G. Grindhammer[26], A. Gruber[26], C. Gruber[16], J. Haack[35], D. Haidt[11], L. Hajduk[6], O. Hamon[29], M. Hampel[1], M. Hapke[11], W.J. Haynes[5], J. Heatherington[20], G. Heinzelmann[13], R.C.W. Henderson[18], H. Henschel[35], I. Herynek[30], M.F. Hess[26], W. Hildesheim[11], P. Hill[5], K.H. Hiller[35], C.D. Hilton[22], J. Hladký[30], K.C. Hoeger[22], M. Höppner[8], R. Horisberger[33], V.L. Hudgson[3], Ph. Huet[4], M. Hütte[8], H. Hufnagel[14], M. Ibbotson[22], H. Itterbeck[1], M.-A. Jabiol[9], A. Jacholkowska[27], C. Jacobsson[21], M. Jaffre[27], J. Janoth[15], T. Jansen[11], L. Jönsson[21], D.P. Johnson[4], L. Johnson[18], H. Jung[29], P.I.P. Kalmus[20], D. Kant[20], R. Kaschowitz[2], P. Kasselmann[12], U. Kathage[16], J. Katzy[14], H.H. Kaufmann[35], S. Kazarian[11], I.R. Kenyon[3], S. Kermiche[23], C. Keuker[1], C. Kiesling[26], M. Klein[35], C. Kleinwort[13], G. Knies[11], W. Ko[7], T. Köhler[1], J.H. Köhne[26], H. Kolanoski[8], F. Kole[7], S.D. Kolya[22], V. Korbel[11], M. Korn[8], P. Kostka[35], S.K. Kotelnikov[25], T. Krämerkämper[8], M.W. Krasny[6,29], H. Krehbiel[11], D. Krücker[2], U. Krüger[11], U. Krüner-Marquis[11], H. Küster[2], M. Kuhlen[26], T. Kurča[17], J. Kurzhöfer[8], B. Kuznik[34], D. Lacour[29], F. Lamarche[28], R. Lander[7], M.P.J. Landon[20], W. Lange[35], P. Lanius[26], J.-F. Laporte[9], A. Lebedev[25], F. Lehner[11], C. Leverenz[11], S. Levonian[25], Ch. Ley[2], G. Lindström[12], J. Link[7], F. Linsel[11], J. Lipinski[13], B. List[11], G. Lobo[27], P. Loch[27], H. Lohmander[21], J.W. Lomas[22], G.C. Lopez[20], V. Lubimov[24], D. Lüke[8,11], N. Magnussen[34], E. Malinovski[25], S. Mani[7], R. Maraček[17], P. Marage[4], J. Marks[23], R. Marshall[22], J. Martens[34], G. Martin[13], R. Martin[11], H.-U. Martyn[1], J. Martyniak[27], S. Masson[2], T. Mavroidis[20], S.J. Maxfield[19], S.J. McMahon[19], A. Mehta[5], K. Meier[15], D. Mercer[22], T. Merz[35], A. Meyer[11], C.A. Meyer[37], H. Meyer[34], J. Meyer[11], A. Migliori[28], S. Mikocki[6], D. Milstead[19], F. Moreau[28], J.V. Morris[5], E. Mroczko[6], G. Müller[11], K. Müller[11], P. Murín[17], V. Nagovizin[24], R. Nahnhauer[35], B. Naroska[13], Th. Naumann[35], P.R. Newman[3], D. Newton[18], D. Neyret[29], H.K. Nguyen[29], T.C. Nicholls[3], F. Niebergall[13], C. Niebuhr[11], Ch. Niedzballa[1], R. Nisius[1], G. Nowak[6], G.W. Noyes[5], M. Nyberg-Werther[21], M. Oakden[19], H. Oberlack[26], U. Obrock[8], J.E. Olsson[11], D. Ozerov[24], E. Panaro[11], A. Panitch[4], C. Pascaud[27], G.D. Patel[19], E. Peppel[35], E. Perez[9], J.P. Phillips[19], Ch. Pichler[12], A. Pieuchot[23], D. Pitzl[36], G. Pope[7], S. Prell[11], R. Prosi[11], K. Rabbertz[1], G. Rädel[11], F. Raupach[1], P. Reimer[30], S. Reinshagen[11], P. Ribarics[26], H. Rick[8], V. Riech[12], J. Riedlberger[36], S. Riess[13],

M. Rietz[2], E. Rizvi[20], S.M. Robertson[3], P. Robmann[37], H.E. Roloff[35], R. Roosen[4], K. Rosenbauer[1], A. Rostovtsev[24], F. Rouse[7], C. Royon[9], K. Rüter[26], S. Rusakov[25], K. Rybicki[6], R. Rylko[20], N. Sahlmann[2], D.P.C. Sankey[5], P. Schacht[26], S. Schiek[13], S. Schleif[15], P. Schleper[14], W. von Schlippe[20], D. Schmidt[34], G. Schmidt[13], A. Schöning[11], V. Schröder[11], E. Schuhmann[26], B. Schwab[14], G. Sciacca[35], F. Sefkow[11], M. Seidel[12], R. Sell[11], A. Semenov[24], V. Shekelyan[11], I. Sheviakov[25], L.N. Shtarkov[25], G. Siegmon[16], U. Siewert[16], Y. Sirois[28], I.O. Skillicorn[10], P. Smirnov[25], J.R. Smith[7], V. Solochenko[24], Y. Soloviev[25], J. Spiekermann[8], S. Spielman[28], H. Spitzer[13], R. Starosta[1], M. Steenbock[13], P. Steffen[11], R. Steinberg[2], B. Stella[32], K. Stephens[22], J. Stier[11], J. Stiewe[15], U. Stößlein[35], K. Stolze[35], J. Strachota[30], U. Straumann[37], W. Struczinski[2], J.P. Sutton[3], S. Tapprogge[15], V. Tchernyshov[24], C. Thiebaux[28], G. Thompson[20], P. Truöl[37], J. Turnau[6], J. Tutas[14], P. Uelkes[2], A. Usik[25], S. Valkár[31], A. Valkárová[31], C. Vallée[23], D. Vandenplas[28], P. Van Esch[4], P. Van Mechelen[4], A. Vartapetian[11,38], Y. Vazdik[25], P. Verrecchia[9], G. Villet[9], K. Wacker[8], A. Wagener[2], M. Wagener[33], A. Walther[8], G. Weber[13], M. Weber[11], D. Wegener[8], A. Wegner[11], H.P. Wellisch[26], L.R. West[3], S. Willard[7], M. Winde[35], G.-G. Winter[11], C. Wittek[13], A.E. Wright[22], E. Wünsch[11], N. Wulff[11], T.P. Yiou[29], J. Žáček[31], D. Zarbock[12], Z. Zhang[27], A. Zhokin[24], M. Zimmer[11], W. Zimmermann[11], F. Zomer[27], K. Zuber[15], and M. zurNedden[37] [1]

I. Physikalisches Institut der RWTH, Aachen, Germany[a]
[2] III. Physikalisches Institut der RWTH, Aachen, Germany[a]
[3] School of Physics and Space Research, University of Birmingham, Birmingham, UK[b]
[4] Inter-University Institute for High Energies ULB-VUB, Brussels; Universitaire Instelling Antwerpen, Wilrijk; Belgium[c]
[5] Rutherford Appleton Laboratory, Chilton, Didcot, UK[b]
[6] Institute for Nuclear Physics, Cracow, Poland[d]
[7] Physics Department and IIRPA, University of California, Davis, California, USA[e]
[8] Institut für Physik, Universität Dortmund, Dortmund, Germany[a]
[9] CEA, DSM/DAPNIA, CE-Saclay, Gif-sur-Yvette, France
[10] Department of Physics and Astronomy, University of Glasgow, Glasgow, UK[b]
[11] DESY, Hamburg, Germany[a]
[12] I. Institut für Experimentalphysik, Universität Hamburg, Hamburg, Germany[a]
[13] II. Institut für Experimentalphysik, Universität Hamburg, Hamburg, Germany[a]
[14] Physikalisches Institut, Universität Heidelberg, Heidelberg, Germany[a]
[15] Institut für Hochenergiephysik, Universität Heidelberg, Heidelberg, Germany[a]
[16] Institut für Reine und Angewandte Kernphysik, Universität Kiel, Kiel, Germany[a]
[17] Institute of Experimental Physics, Slovak Academy of Sciences, Košice, Slovak Republic[f]
[18] School of Physics and Chemistry, University of Lancaster, Lancaster, UK[b]
[19] Department of Physics, University of Liverpool, Liverpool, UK[b]
[20] Queen Mary and Westfield College, London, UK[b]
[21] Physics Department, University of Lund, Lund, Sweden[g]
[22] Physics Department, University of Manchester, Manchester, UK[b]
[23] CPPM, Université d'Aix-Marseille II, IN2P3-CNRS, Marseille, France
[24] Institute for Theoretical and Experimental Physics, Moscow, Russia
[25] Lebedev Physical Institute, Moscow, Russia[f]
[26] Max-Planck-Institut für Physik, München, Germany[a]
[27] LAL, Université de Paris-Sud, IN2P3-CNRS, Orsay, France
[28] LPNHE, Ecole Polytechnique, IN2P3-CNRS, Palaiseau, France
[29] LPNHE, Universités Paris VI and VII, IN2P3-CNRS, Paris, France
[30] Institute of Physics, Czech Academy of Sciences, Praha, Czech Republic[f,h]
[31] Nuclear Center, Charles University, Praha, Czech Republic[f,h]

[32] INFN Roma and Dipartimento di Fisica, Universita "La Sapienza", Roma, Italy

[33] Paul Scherrer Institut, Villigen, Switzerland

[34] Fachbereich Physik, Bergische Universität Gesamthochschule Wuppertal, Wuppertal, Germany[a]

[35] DESY, Institut für Hochenergiephysik, Zeuthen, Germany[a]

[36] Institut für Teilchenphysik, ETH, Zürich, Switzerland[i]

[37] Physik-Institut der Universität Zürich, Zürich, Switzerland[i]

[38] Visitor from Yerevan Phys.Inst., Armenia

1   Introduction

With the ep-collider HERA the investigation of weak charged currents, extensively studied in fixed target experiments[1], has been resumed at a distance scale at which the propagator of the charged weak boson W plays a prominent role[2, 3]. The operation of HERA in 1994 was started with e^- beams and was then switched to e^+ beams allowing considerably increased currents. This opens the possibility to study simultaneously W^+ and W^- induced processes at very high energies in analogy to low energy neutrino and antineutrino scattering.

This article presents the first measurement of the total cross section $e^+p \to \overline{\nu}_e +$ hadrons and an update of the previously measured total cross section for $e^-p \to \nu_e +$ hadrons [2]. The simplicity of the analysis described in the previous publication is maintained. Charged current events at 4-momentum transfer squared Q^2 of order 3000 GeV^2 have the outstanding signature of high transverse momentum hadron systems which appears unbalanced due to the undetected final state neutrino (see figure 1). This feature makes the visible vector transverse momentum sum (V) a simple and efficient discriminant for such events in getting a clean charged current event sample. Data with $V >$ 25 GeV were selected. As the e^+p cross section (a few 10 pb) is less than half the e^-p cross section, while the background situation remains unaltered, the background estimation methods previously described had to be somewhat refined. In particular, a detailed study is presented on the effect of incoming interacting muons and of photon-proton interactions. These latter are significant as they are associated with large cross sections. The efficiency and correction factors are evaluated directly from data wherever possible.

The requirement that V be large simplifies the interpretation of the data in several ways. It enhances the sensitivity to the W propagator ($Q^2 > 625$ GeV^2), it forces Bjorken-x to be larger than 0.03 and excludes regions in which radiative corrections are large, ensuring that the prediction of the cross sections is theoretically reliable. From the measured cross sections their ratio is derived. It is sensitive to the ratio D/U of the integrated d and u quark distributions as well as the helicities of the $W^{\pm}$.

2   Experimental conditions

2.1   HERA

This analysis is based on data taken at the ep-collider HERA in 1994. The integrated luminosities for e^- and e^+ running were 0.36 and 2.70 pb^{-1} respectively. The beam energies were 27.6 GeV for electrons and positrons, and 820 GeV for protons. HERA was operated with 168 electron and 170 proton bunches. 156 bunches were colliding, separated from each other by 96 ns. The width of the interaction region is determined by the length of the proton bunch and was found to be $\sigma_{\mathrm{zvtx}} = 10$ cm.

2.2   The H1 detector

A detailed description of the H1 detector and its performance can be found in [4]. Below only those aspects which are relevant to the measurement of the total charged current cross sections are discussed.
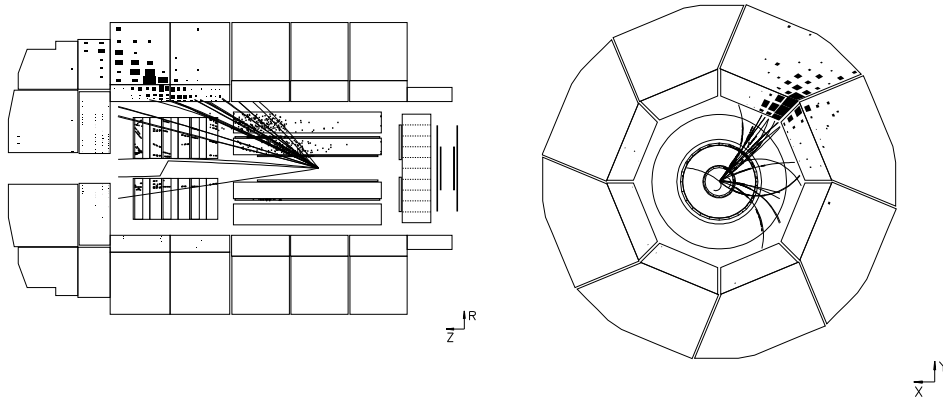
4

Figure 1: *A candidate for the process* $e^+p \to \overline{\nu}_e + \text{hadrons}$ *with* Q^2 *of about 20000 GeV*^{2} *and* $Bjorken - x$ *of about 0.4 recorded in the H1 detector. The views along (the proton beam enters from the right, the positron beam from the left) and perpendicular to the beam are shown.*

.

The energy of the hadronic final state is measured in the highly segmented liquid argon (LAr) calorimeter [5], which cover the polar angular direction between 4° and 153° with respect to the proton beam direction taken to be the $+z$-direction. The LAr calorimenter consists of an electromagnetic section with lead absorber and a hadronic section with stainless steel absorber. The total depth of the electromagnetic part varies with polar angle between 20 and 30 radiation lengths, whereas the total depth of both calorimeters combined varies between 4.5 and 8 interaction lengths. The calibration of the LAr calorimeter was obtained from test beam measurements using electrons and pions [4, 5, 6]. The resolution for pions was found to be $\sigma(E)/E \approx 0.5/\sqrt{(E/\text{GeV})} \oplus 0.02$. The hadron energy scale was verified to 5% from studies of the transverse momentum balance in neutral current deep inelastic scattering events. The energy scale for electrons was verified to 3% using the double angle method[8]. For trigger purposes the LAr calorimeter is read out in a much coarser granularity via FADCs. This information provides a fast trigger decision based on the energy deposition and on the topology of the event. The analysis of the FADC spectra allows the determination of the time at which the event took place with an accuracy of $10 - 30$ ns, sufficient to determine the bunch crossing within which the event occurred.

Charged particles in the polar angle range $15^o - 165^o$ are measured in the central drift chamber (CJC) and used to determine an event vertex. The time of occurrence of each event is determined with a precision of 1 ns from tracks which cross the CJC sense wire planes. The CJC is supplemented by several layers of proportional chambers providing fast trigger decisions based on tracks.

Both, the LAr calorimeter and the central jet drift chamber are surrounded by a super-conducting solenoid. The iron yoke which returns the magnetic flux is instrumented with streamer tubes and is used as muon detector. The streamer tubes are read out in digital mode for trigger purposes and muon track identification and in analog mode for energy reconstruction of particles passing through the LAr calorimeter. The timing of the muon trigger system is precise enough (~ 20 ns) to assign events to a unique bunch crossing.

5

A time-of-flight (ToF) system built out of two scintillator planes is used to veto background caused by proton beam-gas and beam-wall interactions upstream of the detector.

The luminosity system measures the rate of small angle Bremsstrahlung processes [7]. It consists of two crystal calorimeters at $z = -33$ m and $z = -103$ m from the nominal interaction point, the first to detect the scattered electron or positron *(e-tagger)*, the other to detect the emitted photon. The e-tagger is also used to detect the scattered lepton in γp interactions.

2.3 Event selection

Two observables, the *scalar* (S) and *vector* (V) transverse momentum sums, are used to characterise charged current events at large values of the 4-momentum transfer square :

$$
\begin{aligned}
S &\equiv \sum_i |\vec{p}_{\perp i}| \\
V &\equiv |\sum_i \vec{p}_{\perp i}| \,.
\end{aligned}
$$

S and V correspond to the *total transverse energy* and the *missing transverse energy* in each event. The computation of these quantities is straightforward, requiring only the calorimeter cell energies (index i) and positions, and the event vertex position. Charged current events are characterised by large values of S and V. Note that by definition $S \geq V$. The main selection criterion for charged current candidates is based on the observable V.

The event selection proceeds in several steps. The hardware trigger condition for charged current events (CC) has to be fulfilled. This consists of a coincidence of the calorimeter V-trigger and the z-vertex time signal in anti-coincidence with the ToF-veto signal. The calorimeter V-trigger calculates the vector sum of the transverse momenta based on the coarsely segmented calorimeter trigger read out and requires $V_{\text{trig}} > 6$ GeV. The z-vertex time signal identifies the event time and requires at least 3 out of 4 proportional chamber layers hit. A fast online reconstruction verifies the hardware trigger decision and rejects obvious background from cosmic and beam halo muons, beam-gas, and beam-wall interactions.

An event vertex must have been reconstructed from tracks detected in the central drift chamber. The vertex is required to lie in the range of $\Delta z = \pm 35$ cm around the nominal interaction point.

The vector sum V of the transverse momenta, reconstructed from the LAr calorimeter cells is required to exceed 25 GeV, well above the initial threshold V_{trig}.

In total 1133 candidates satisfied the CC selection criteria.

3 Background

Two sources of background to the charged current events are considered: events induced by incoming interacting muons and background from ep interactions. They are discussed in the two subsequent sections.

6

Classification	*Time*-id	no *Time*-id
Topo-id	773	272
no *Topo*-id	18	70

Table 1: *Classification of the 1133 events according to topology (Topo) and timing (Time) properties.*

3.1 Muon-induced background

The charged current selection described above may be satisified by cosmic ray or proton beam halo events in which the muon interacts with the detector. These radiative interactions generate electromagnetic showers. A careful analysis of the topology of these showers, and their timing with respect to the beam crossing, reveals characteristics that enable the identification and removal of such events. This analysis is described briefly here and in more detail in appendix A.

Halo muons : A high flux of muons accompanies the proton beam and some of these traverse the detector parallel to the beam line. There are two possibilities to fulfill the CC selection criteria :
(a) The muon interacts in the LAr calorimeter, while the track of the penetrating muon continues over the entire longitudinal range of the calorimeter at constant distance from the beam line. The secondaries deposit sufficient energy either in the electromagnetic or hadronic part of the calorimeter and a charged secondary satisfies the vertex criterion.
(b) The halo muon sets the energy trigger, while a simultaneous beam related interaction occurred satisfying the vertex requirement. Such events are called *superimposed event.*

Cosmic muons : Cosmic ray muons penetrate the detector at all angles. Their time of passage is unrelated to the time of the beam interaction. Again, there are two ways in which such events may fulfill the CC selection criteria :
(a) the muon interacts in the detector such that enough energy is deposited in the calorimeter and that a secondary charged particle accidentally fulfills the vertex requirement
(b) the muon is superimposed over a beam induced interaction (beam gas or γp), while the "underlying" event satisfies the vertex requirement.

Muon induced background may be identified in two independent ways by applying topological and timing criteria with the result of being identified by both, only one, or none of these criteria, as summarised in table 1. As the topological and timing criteria are independent, the efficiency of the background identification procedure may also be determined. Removing events identified as background by either or both of the above criteria leaves a sample of 70 events. The number of muon associated events remaining in this sample is $(272 \times 18)/773 \approx 6 \pm 2$.

In order to check the above procedure, the 88 candidates left untagged by the topological information are subjected in a visual scan to a quality control. Of these events 26 events were uniquely verified as being due to incoming muons in agreement with the number expected from the above analysis of 18 tagged and 6 from the statistical estimate.

The visual scan also revealed 6 obviously misclassified neutral current events in the CC sample, in which the electron or positron candidate or the hadron shower point to a crack in the calorimeter, and 1 event due to noise in the calorimeter. These are unambiguous background

events and are removed from the sample. Furthermore, there are 2 events containing isolated high $p_\perp$ final state leptons, one with a muon[15] and another with an electron. An obvious source of such events is W production with subsequent leptonic decay. Events of this type are interesting in their own right and are excluded from the CC sample.

To summarise, after the background subtraction described above, the charged current sample consists of 53 candidates, 12 within the e^- runs and 41 within the e^+ runs. The position of these events in the V-S plane is shown in fig. 2, the *signal region* being that with $V > 25$ GeV. The
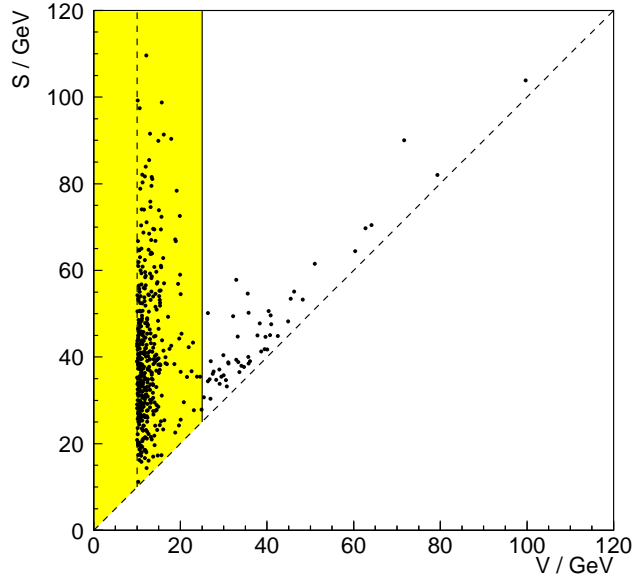
Figure 2: *Selected events in the V-S plane for $V > 10$ GeV. The* signal region *is defined by $V > 25$ GeV.*

expected correlation between V and S for CC events is observed. An outstanding CC event is shown in figure 1. The region with $10 < V < 25$ GeV is referred to as *control region* in the following.

3.2 ep-induced background

Three sources of ep interaction induced background is considered: beam-gas or beam-wall interactions; neutral current interactions in which the electron or positron is not detected and γp interactions. The large transverse momentum imbalance required ($V > 25$ GeV) eliminates the beam-gas as well as the beam-wall background, while the other contaminations are strongly suppressed.

A neutral current interaction with large Q^2 may fake a charged current interaction, if the electron or positron remain undetected. This may occur if the final state lepton is emitted close to the beam pipe ($\theta_e < 4°$) or it hits a region of dead material in the detector. As may be seen from figure 3, which shows the polar angle distribution of a reference sample of neutral current events, the former background is negligible with current data. The latter background was eliminated by visual inspection.
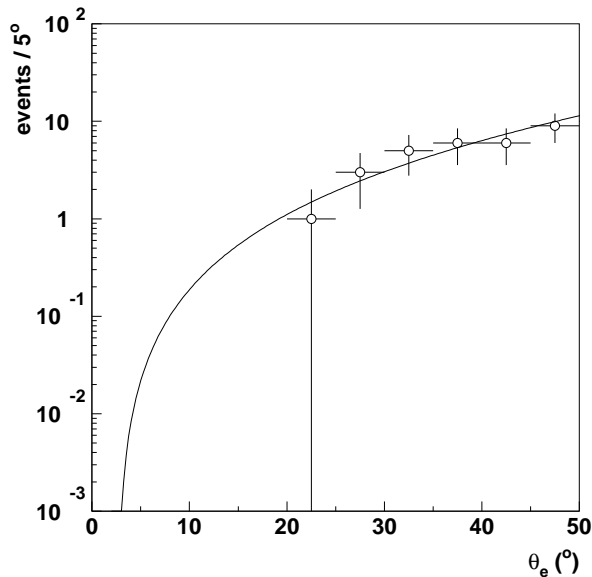
Figure 3: *Angular distribution of the final state electron for a neutral current reference sample with $V > 25$ GeV. The solid line is the theoretical expectation used for extrapolation to small angles. The calorimeter starts at 4°.*

Neutral current interactions at very small Q^2 may be considered as being due to the interaction of a quasi real photon with the proton (γp). Their cross section is very large. The electron remains usually undetected. Photon proton interactions with large enough transverse energy show up mainly as planar two jet configurations which are balanced in transverse momentum, thus the vast majority of the γp events have $V \approx 0$ and do not satisfy the requirement that $V > 25$ GeV. There are nevertheless two effects which may cause a γp event to have significant transverse momentum unbalance. These are particle losses in the beam pipe and the effects of the calorimeter resolution. Both effects are important as verified by Monte Carlo studies. Configurations corresponding to V exceeding the cut off value of 25 GeV require a γp interaction in which the participating partons carry a large proportion of the momentum of the parent particles, resulting also in a large value of the scalar transverse momentum sum S. The rate of such events is strongly suppressed.

In order to assess this background quantitatively the analysis has been extended to a region with a substantially relaxed V cut of 10 GeV, where the detection efficiency for CC events is still reasonably large. For this purpose slightly modified selection criteria and less restrictive trigger requirements were applied. The additional events in this region are shown in figure 2. Their composition is dominated by γp interactions, but contains of course also CC events. Indeed some γp events identify themselves unambiguously by the presence of an isolated final state lepton in the small angle tagging system. Figure 4 shows the V-distribution of all selected events. A steep exponential fall-off is observed for small values of V in contrast to the rather flat distribution at large values of V in the signal region. The behaviour for V above 10 GeV can be well described by the sum of an exponential plus the expected shape of the CC events. The solid line in figure 4 is the result of a fit allowing as free parameters the exponential slope and the normalisations. The fit yields a slope of $-(0.47 \pm 0.03)$ GeV^{-1}. The extrapolation into the signal region above $V = 25$ GeV predicts a background of 0.3 ± 0.1 events within the 53 CC
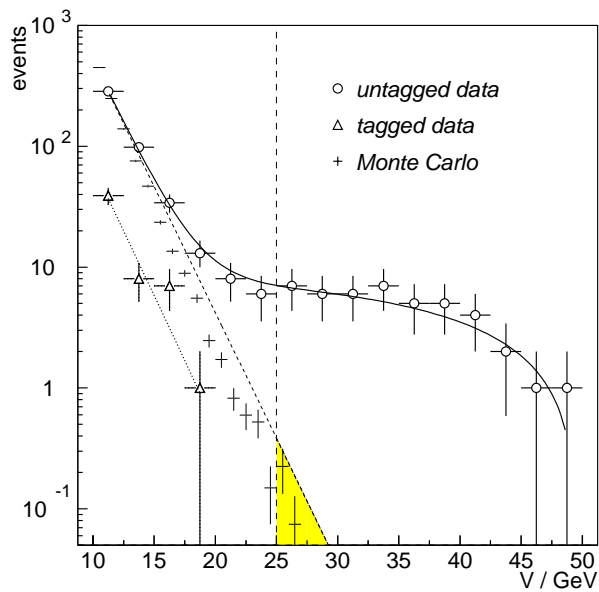
Figure 4: *Distribution of all events in the control and signal region versus V (the vector transverse momentum sum). The data are marked as open circles. The solid line is the result of the fit described in the text. The dashed line shows the γp contribution and its extrapolation into the signal region. Also shown by open triangles are the tagged γp data. The γp Monte Carlo simulation is represented by the small crosses.*

candidates.

As a check figure 4 also shows the predicted behaviour based on a sample of γp events generated using the PYTHIA program package[12]. It is normalised to the data at low V. The exponential shape is supported by direct comparison with tagged γp events as seen in figure 4. The exponential behaviour and the numerical value for the slope agree well with observation corroborating the extrapolation into the signal region.

As a further check the 14 events in the interval between 20 and 25 GeV of the control region have been scanned for topologies consisting of two planar jets. Three such events were found, compatible with the 3.3 γp events predicted by the fit. In conclusion, the background due to γp events is negligible.

4   Corrections

The efficiencies of and corrections arising from the various selection steps are summarised in table 2. These were determined using a NC reference sample, termed *PseudoCC,* which was obtained by removing the electron and requiring for the hadron system the same criteria as for CC candidates. This procedure works well and does not rely on a simulation of CC events. Nontheless, the results were checked using a Monte Carlo simulation and good agreement was found.   The inefficiency in the CC trigger is mainly due to the coarse granularity of the calorimeter trigger read out system. The effective threshold is therefore significantly higher than

Analysis step	Correction factor (e^-)	Correction factor (e^+)
Selection	0.97 ± 0.02	0.97 ± 0.02
Vertex	0.86 ± 0.03	0.87 ± 0.03
CC-trigger	0.90 ± 0.02	0.90 ± 0.02
V-cut	0.94 ± 0.05	0.91 ± 0.07
Total ϵ	0.71 ± 0.05	0.69 ± 0.06

Table 2: *Correction factors to the charged current samples.*
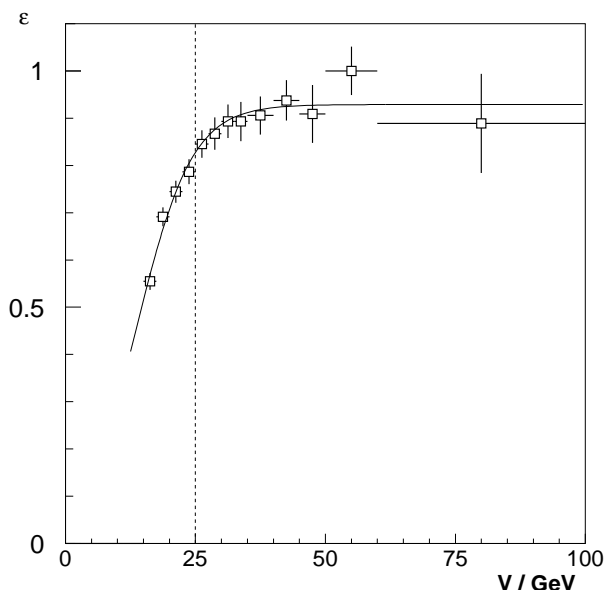
Figure 5: *The charged current trigger efficiency as a function of the vector sum of transverse momenta, V. The squares show the data points and the full line a parametrisation of the threshold curve. The dashed line indicates the analysis cut.*

the nominal one (cf. fig. 5). The efficiency for $V > 25$ GeV is 0.92. An additional inefficiency of 0.02 arises from the track requirement in the trigger. Together with a small inefficiency from the ToF veto condition, the total trigger efficiency was determined to 0.90. A systematic error of 0.02 is given by the limited statistics of the *PseudoCC* sample. The limited vertex efficiency is dominantly of geometrical nature. The acceptance of the central drift chamber falls steeply in the forward area below 30° (cf. fig. 6). The vertex efficiency for events with $V > 25$ GeV is found to be near to 0.9 (see table 2). A small difference between the efficiencies for e^- and e^+ induced charged current events is expected, since the angular spectra of their hadronic final states are different.

The efficiency for the fast online and offline background rejection chain was as well determined from the *PseudoCC* sample and found to be 0.97 ± 0.02.

The reconstructed vector sum of transverse momenta, V, is affected by the apparatus used in the measurement and the details of the method used. The effect of the V-cut is thus experiment dependent and a correction must be applied to obtain results corresponding to the
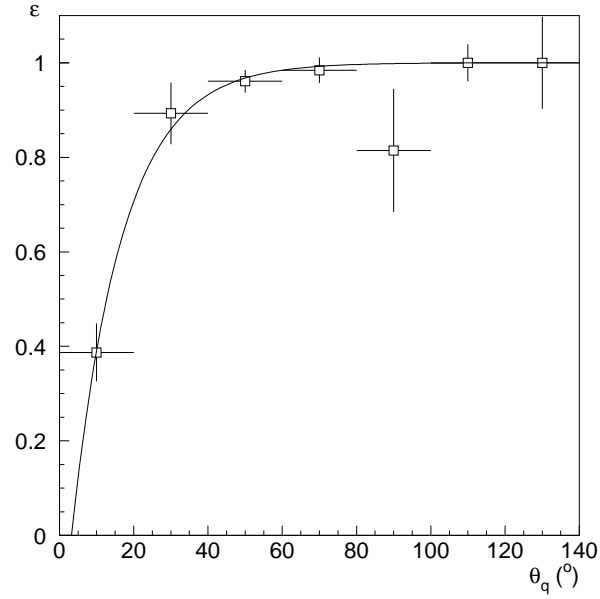
11

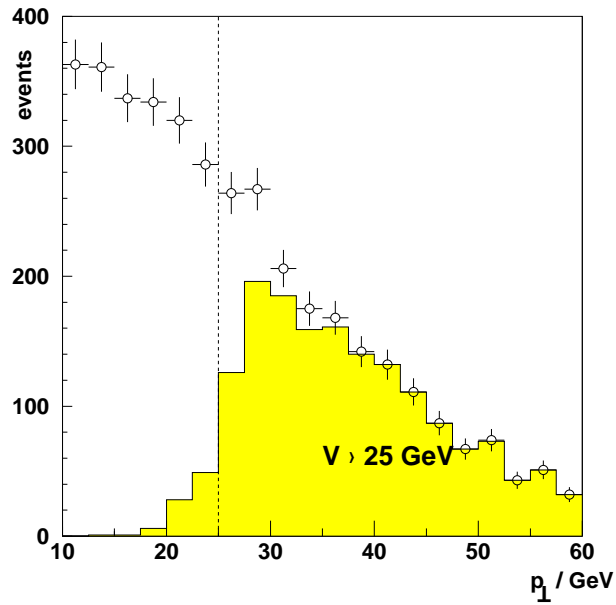Figure 6: *The vertex efficiency as a function of scattering angle of the hadronic final state.*

Figure 7: *Spectrum of the final state neutrino's transverse momentum $p_\perp$ from a MC simulation of e^+p scattering. The crosses show all events, while the shaded histogram shows the distribution for those events with $V > 25$ GeV. The dashed line represents the $p_\perp$-cut illustrating gain and loss.*

true transverse momentum $(p_\perp)$ of the final state neutrino. Figure 7 illustrates how the V-cut correction accounts for gains and losses due to resolution, radiative effects, and particles escaping detection. The calculation of the correction factor relies on MC simulation and yields 0.94 and 0.91 for the e^- and e^+ running, respectively. The migration of events depends strongly on the energy scale of the LAr calorimeter. For the estimated $\pm 5\%$ hadron energy scale error the migration efficiency changes by 0.05 and 0.07 for e^- and e^+. These uncertainties are accounted for in the systematic error. Theoretical uncertainties in the hadronisation model used in the simulation yield an additional error of 0.01.

5 Results and conclusion

The charged current cross sections for $p_\perp > 25$ GeV are then calculated according to:

$$\sigma = \frac{N}{\mathcal{L}\epsilon}.$$

The data samples used correspond to an integrated luminosity of $\mathcal{L} = 2.70 \pm 0.05\,\text{pb}^{-1}$ for e^+ and $\mathcal{L} = 0.36 \pm 0.01\,\text{pb}^{-1}$ for e^-. The statistical errors of these measurements are negligible. The systematic errors arise primarily from uncertainties as to the acceptance of the luminosity system under varying beam conditions. Considerable progress has been made in understanding these uncertainties since 1993. The observed numbers of 12 e^- and 41 e^+ induced charged current events, with the corrections listed in table 2, give cross sections of:

$$\sigma \quad (e^-p|p_\perp > 25\,\text{GeV}) = 46.6 \pm 13.5 \pm 3.5\,\text{pb}$$
$$\sigma \quad (e^+p|p_\perp > 25\,\text{GeV}) = 21.9 \pm\ \ 3.4 \pm 2.0\,\text{pb}$$

where the first error is statistical and the second error includes all systematic effects added in quadrature. The systematic uncertainties of the two results are strongly correlated.

The measured total e^-p cross section agrees well with value previously published by the H1 Collaboration[2] as well as with the measurement of the ZEUS Collaboration[3]. Combination of the earlier H1 result with that discussed here, taking into account common systematics (the correlation coefficient is 0.70) and the increased electron beam energy gives:

$$\sigma(e^-p|p_\perp > 25\,\text{GeV}) = 50.6 \pm 10.9\,\text{pb}$$

where the error includes both statistical and systematic uncertainties. The correlation coefficient of the systematic errors of the combined e^-p and the e^+p measurements is 0.16, which leads to a slight tilting of the error ellipse in the $\sigma(e^-) - \sigma(e^+)$ plane shown in fig. 8. This figure also shows the theoretical expectation as a function of the W propagator mass, calculated using the HERACLES[13] package with the inclusion of electroweak radiative effects [9]. The sensitivity of both the e^-p and e^+p cross sections to the mass value assumed for the W-propagator is clearly visible. The best value of the propagator mass inferred from this figure agrees within 90 % C.L. with the known resonance mass of 80.2 GeV [14], while its uncertainty is about 15 GeV.

The charged current event sample includes 2 events with isolated photons of transverse momentum larger than 2 GeV, consistent with the theoretical expectation.

The ratio R_e of the two measured charged current cross sections is

$$\frac{\sigma(e^+p|p_\perp > 25\,\text{GeV})}{\sigma(e^-p|p_\perp > 25\,\text{GeV})} = 0.43 \pm 0.11,$$
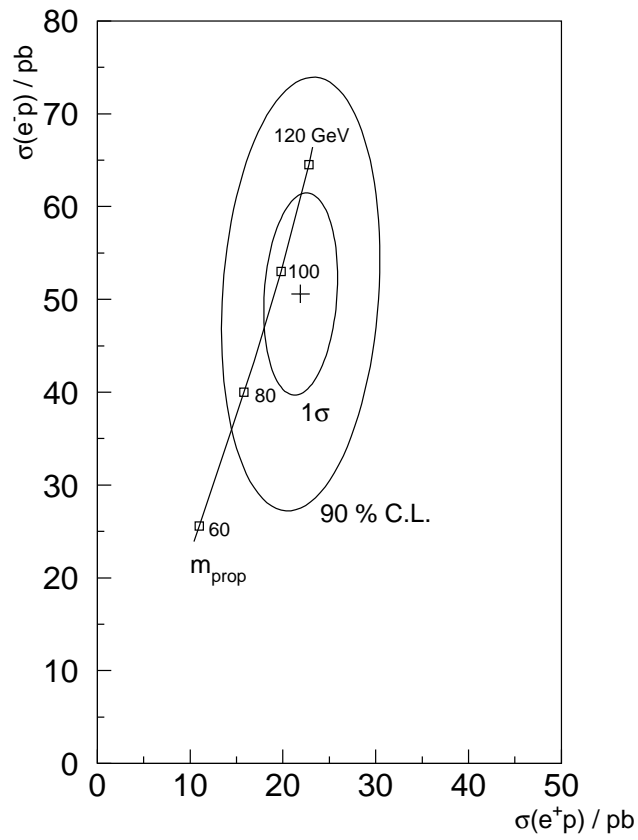
Figure 8: *The measured e^-p and e^+p cross sections compared with the predicted cross section as a function of the W propagator mass (m_{prop}). The two ellipses correspond to the 39.4 % (1σ) and 90 % CL contours.*

where the common systematic uncertainties drop out.

The quark-parton model explains qualitatively the value of the cross section ratio R_e in terms of the relevant $e^\pm$ quark and antiquark subprocesses mediated by the weak vector bosons $W^\pm$. A good approximation is :

$$R_e \approx \frac{\sigma(e^+d) + \sigma(e^+\overline{u})}{\sigma(e^-u)} = \frac{D}{U}(a_1 + a_0\frac{\overline{U}}{D})$$

where D/U and $\overline{U}/D$ are the ratios of the corresponding integrated parton distributions, whereas $a_1 = \langle(1-y)^2\rangle$ (y being the Bjorken scaling variable) and $a_0 = \langle1\rangle$ account for the W helicities averaged over the appropriate parton distributions [16]. While the sea in the proton contributes little to e^-p scattering, its contribution to e^+p scattering is of the same size as that of the one of the valence d-quark. Although the W propagator strongly affects each cross section separately, the effect on cross section ratios is much reduced.

Finally, the measured ratio R_e can be compared with the analogous quantity, the ratio R_ν, measured previously in fixed target neutrino experiments [1] at much lower energies :

$$\frac{\sigma(\nu_\mu p \to \mu^- + \text{hadrons})}{\sigma(\overline{\nu}_\mu p \to \mu^+ + \text{hadrons})} = 0.97 \pm 0.04.$$

Both R_e and R_ν are the ratio of a W^+ and a W^- induced interaction on a proton target, however at vastly different energies. With the approximation of R_ν by $D/U \cdot (a_1 + a_0 \cdot \overline{D}/U)^{-1}$, the numerical difference between R_e and R_ν can be understood as the interplay of the W helicities and the quark flavors. The large difference in the interaction energies modifies the averages over the angular distributions (a_1 and a_0) and influences considerably the importance of the sea in the proton.

The quantitative comparison of the two ratios is done without approximations. R_e is first extrapolated to $p_\perp = 0$ implying the use of the structure functions also at values of Bjorken-x below 0.03. The MRS-H [10] parton distributions are used. They are based on HERA data as well as low energy fixed target measurements. They also agree well with measurements at the TEVATRON[11] which are sensitive to the u and d quark distributions. The extrapolation in $p_\perp$ down to 0 emphasises the contribution of the sea and increases the D/U ratio by about 20 %. The ratio R_e after extrapolation to $p_\perp = 0$ becomes 0.59 ± 0.15 and can be converted into R_ν by calculating the effect of replacing the e by a ν and by extrapolating from HERA energies corresponding to about 48 TeV, if seen as fixed target experiment, down to SPS energies of the order of 100 GeV. The ratio R_e after applying all relevant conversion factors becomes 1.15 ± 0.30 in good agreement with $R_\nu = 0.97 \pm 0.04$ measured in neutrino experiments.

Appendix : Incoming muon background

A detailed account is presented on the characteristics and treatment of the background originating from incoming muons.

Characteristics

Incoming muons appear either as halo or as cosmic muons with well defined and unique topological and timing properties which may serve to a twofold classification.

From the topological point of view the 1133 events are attributed to three classes (see table 3) :

The **Halo** class consists of 509 events identified by the halo finder. The principle of halo finders is to check for an energy distribution in the LAr calorimeter which is very localised in the $r - \phi$-plane while having large spread in the z-direction thus being typical for a particle traversing the detector parallel to the beam. This information is combined with a requirement of muon tracks or energy deposits in the instrumented iron yoke.

The **Cosmic** class consists of 536 events identified by the cosmic but not the halo finder. Cosmic finders use moments of energy distributions in the calorimeters, local properties (like direction and shape) of calorimeter showers as well as tracks and energy deposits in the muon detectors to identify cosmic muons which deposit large amounts of energy in the detector.

The **CC** class consisting of 88 charged current candidates contains the genuine CC events together with a small background of incoming muons due to the inefficiencies of the finders.

The CC class appears as the rest class of events neither assigned to the halo nor the cosmic class. The three classes are disjoint. The scatter plot (figure 9 a) of the 1133 events in terms of the timing of the Jet chamber and the LAr calorimeter shows two prominent time bands. To be specific, two time bands I_0 and I_1 are defined by $T_{CJC} = 0.0 \pm 0.1$ in units of the bunch crossing time and by $|T_{CJC} - T_{LAr}| < 0.7$ respectively. The intrinsic timing accuracy of the Jet chamber is better than 1 ns. The larger band of ± 0.1 ensures independence of assumptions on the origin and direction of the particles. The upper limit of 0.7 comfortably takes into account the variations of the LAr timing resolution over the entire calorimeter. The two bands distinguish events according to whether they occur correlated or uncorrelated with the bunch crossings. Thus, each event can then be assigned in an independent way to exactly one of four time windows :

342 **prompt** events (P) in the intersect of I_0 and I_1

414 **uncorrelated** events (U), i.e. not prompt events in the band I_1

344 **superimposed** events (S), i.e. not prompt events in the band I_0

33 **non assigned** events (N) belonging neither to I_0 nor to I_1

The U, S and N classes contain only background events, whereas genuine CC events belong to the P class. All classes are again disjoint by construction.

The combination of the two classification schemes leads to 12 disjoint subclasses as listed in table 3 and shown in figure 9.
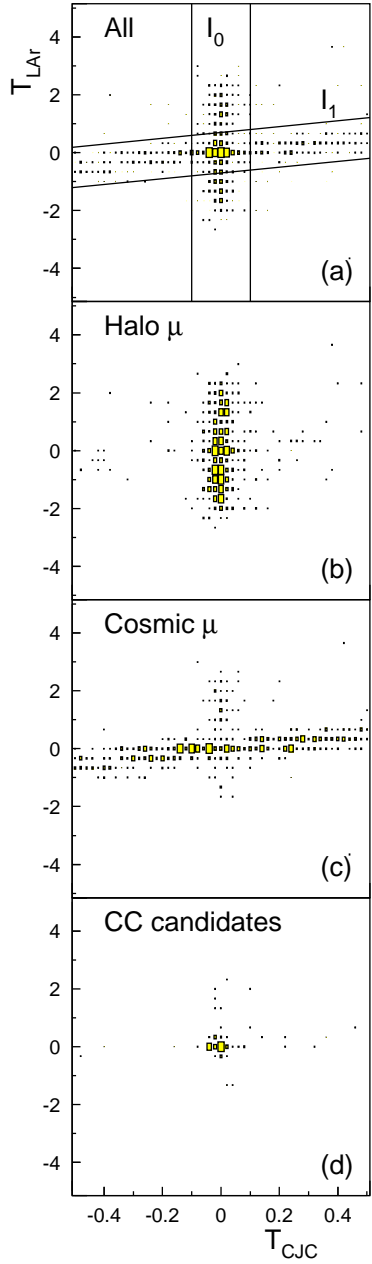
Figure 9: *The time structure of all events (a), halo events(b), cosmic muon events (c) and CC candidates (d) is shown as a function of the CJC and the LAr timing. All times are given in units of 1 bunch crossing (96 ns). The two bands I_0 and I_1 are explained in the text.*
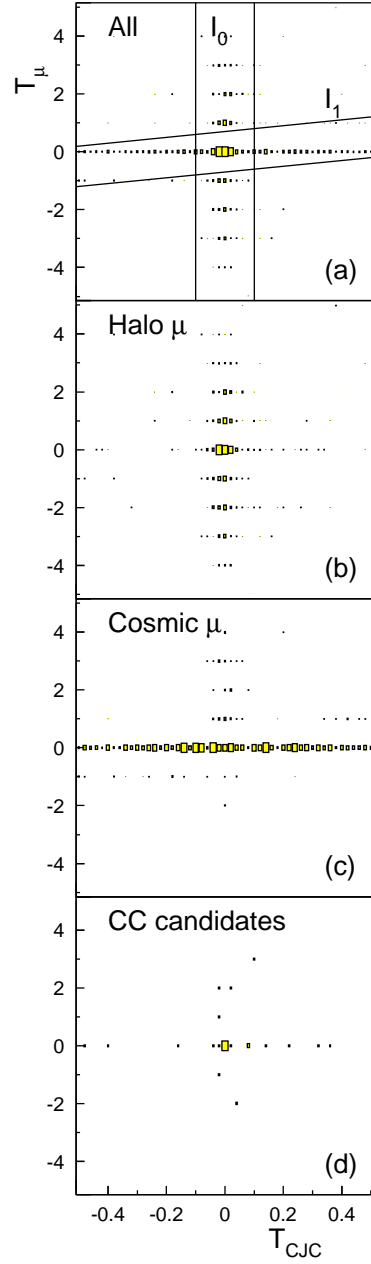
Figure 10: *The time structure of all events with a signal in the muon detector (a), halo events(b), cosmic muon events (c) and CC candidates (d) is shown as a function of the CJC and the μ timing. All times are given in units of 1 bunch crossing (96 ns). The two bands I_0 and I_1 are explained in the text.*

Classification	All	P	U	S	N
All	1133	342	414	344	33
Halo	509	159	38	287	25
Cosmics	536	113	366	50	7
CC candidates	88	70	10	7	1

Table 3: *Event classification according to topology and CJC and LAr timing. The abbreviations P,U,S,N stand for prompt, uncorrelated, superimposed, non assigned events.*

Classification	all	μ corr(seen)	P	U	S	N
halo	509	509 (409)	135.7 (109)	34.8(28)	304.9 (245)	33.6 (27)
cosmics	536	536 (508)	112.9 (107)	364.0(345)	48.5 (46)	10.6 (10)
CC candidates	88	26.3 (23)	11.4 (10)	8.2 (7)	5.7 (5)	1.1 (1)

Table 4: *Event classification according to topology and CJC and μ timing corrected(uncorrected) for μ detection efficiency.*

Determination of the background due to incoming muons

Table 3 shows that the topological and the timing information alone efficiently reduce the background. It is their simultaneous application which allows to disentangle the incoming muon background quantitatively.

Halo events are expected to populate the I_0 band. This is verified by figure 9 b. Similarly, cosmic muons occur at the same time as recorded by both subdetectors, but unrelated with the bunch crossing time, i.e. they are expected to populate the I_1 band, as borne out by figure 9 c.

The observed number of prompt cosmic muon events matches well with the expected number calculated from the side bands. This holds for the non superimposed halos as well. It is interesting to note that figure 9 d is dominated by prompt events, the expected genuine CC events, but still contaminated with both halo and cosmic muon events, as inferred from the observed 18 nonprompt events. In fact, the observed number of superimposed and uncorrelated events in the three topological classes (see table 3) allows the calculation of the inefficiency of the halo and cosmic filters yielding $1 - \epsilon = 0.02 \pm 0.01$ and 0.03 ± 0.01 respectively. The 70 prompt CC candidates have therefore a residual background of 6 ± 2 events due to incoming muons.

The timing of the muon trigger system allows an independent check of the above. Since CC events do not have muons (apart from events containing decay muons), the use of the muon timing checks directly the background due to incoming muons. Although the precise muon timing of 20 ns is truncated to the corresponding bunch crossing time and is not available for all incoming muons due to the inefficiency of the muon detection, it spans a wide range of bunch crossings (see figure 9 b). Figure 9 and table 4 repeat the corresponding figure and table with the muon trigger timing replacing the LAr timing. The numbers in table 4 include a correction for muon detection efficiency (80 % for halos and 95 % for cosmics) are very similar to the corresponding numbers in table 3 except of course for the CC class expected to contain

primarily background. The inefficiencies of the filters estimated from table 4 agree with the numbers derived from table 3 and lead to an estimated background of 5 ± 2 events among the 10 observed prompt events which becomes 11.4 events after efficiency correction.

Visual scan

The purpose of the visual scan, as mentioned in section 3, was to check the quality of the 88 events in the CC class and to identify and remove residual background events from the sample.

The 18 non-prompt events of table 3 were indeed found to be due to incoming muons. The remaining 17 prompt background events contain 8 incoming muons (7 cosmic muons and one halo muon) also be compared with the 6 ± 2 events calculated above.

The scan results can also be confronted with the 23 events among the 88 events for which a muon signal is available (table 4). The 13 non-prompt events in this sample were identified in the scan as 10 cosmic and 3 halo muons.

The 5 observed prompt incoming muons (4 cosmic and one halo muon) are in agreement with the statistical estimate of 5 ± 2. Two of the prompt events are identified as CC events which happen to leave a signal in the muon detector either as a result of a single penetrating track or by leakage of the hadronic shower. The full prompt muon signal is then quantitatively explained after accounting for two observed NC events and the peculiar muon event [15].

References

[1] D. Haidt and H. Pietschmann: Landolt-Börnstein New Series I/10, Springer (1988), p.217.

[2] H1 Collaboration, T. Ahmed et al., Phys. Lett. **B 324** (1994) 241

[3] ZEUS Collaboration, M. Derrick et al., DESY Preprint 95-053 (March 1995).

[4] H1 Collaboration, I. Abt et al., *The H1 detector at HERA*, DESY Preprint 93-103 (1993).

[5] H1 Calorimeter Group: B. Andrieu et al., Nucl. Instr. and Meth. **A336** (1993), 460

[6] H1 Calorimeter Group, B. Andrieu et al., Nucl. Instr. and Meth. **A336** (1993), 499 ; ibid. **A350** (1994) 57.

[7] H1 Collaboration, T. Ahmed et al., DESY Preprint 95-24 (accepted by Z. Phys. C)

[8] S. Bentvelsen et al., in Proceedings of the workshop *Physics at HERA*, Hamburg, Oct. 29 − 30, 1991, Vol. 1, p. 23, Eds. W. Buchmüller and G. Ingelman, Hamburg 1992; and K.C. Hoeger, ibid. p. 43.

[9] H. Spiesberger, EPRC91, unpublished program manual, 1991; Nucl.Phys. **B349** (1991) 109; *Precision Electroweak Tests at HERA*, Preprint Univ. Bielefeld, BI-TP 93/03, Jan. 1993, to be publ. in *Precision Tests of the Standard Model*, Advanced Series on Directions in High Energy Physics, World Scientific Publishing Co., Ed. Paul Langacker.

[10] A.D.Martin, R.G.Roberts and W.J.Stirling, Proc. of the Workshop on Quantum Field Theory, Theor. Aspects of HEP, eds. B.Geyer and E.M. Ilgenfritz (1993) 11-26.

[11] CDF Collaboration, F. Abe et al., Phys. Rev. Lett. **74** (1994) 850.

[12] T.Sjöstrand, CERN-TH-6488 (1992), Comp. Phys. Comm. **82** (1994) 74.

[13] A. Kwiatkowski, H. Spiesberger and H.-J. Möhring, *HERACLES. An Event Generator for ep Interactions at HERA Energies Including Radiative Processes*, Version 4.1, in Proceedings of the workshop *Physics at HERA*, Hamburg, Oct. 29 – 30, 1991, Vol. 3, p. 1294, Eds. W. Buchmüller and G. Ingelman, Hamburg 1992.

A. Kwiatkowski, H. Spiesberger and H.-J. Möhring, *HERACLES. An Event Generator for ep Interactions at HERA Energies Including Radiative Processes, Version 4.0*, Comp. Phys. Comm. **69** (1992) 155.

[14] Particle Data Group : Phys. Rev. **D50** (1994) 1191.

[15] H1 Collaboration, T.Ahmed et al., DESY Preprint 94-248 (1994).

[16] V. Brisson et al.:*The measurement of electroweak parameters*, Proceedings of the Workshop "Physics at HERA", eds. W. Buchmüller and G. Ingelman, Hamburg, 1991, Vol. 2, 947.